

10. Nonpolar Cubic III Nitrides: From the Basics of Growth to Device Applications

Donat J. As* and Klaus Lischka

University of Paderborn, Warburger Strasse 100, 33098 Paderborn, Germany;

* d.as@uni-paderborn.de ; phone +49 5251 60 5838; fax +49 5251 60 5843;

ABSTRACT

The Molecular Beam Epitaxy (MBE) of cubic group III-nitrides is a direct way to eliminate polarization effects which may limit the performance of optoelectronic devices containing quantum well or quantum dot active regions. In this paper recent progress with the MBE of phase-pure cubic GaN, AlN and their alloys is reviewed. Reflection high energy electron diffraction (RHEED) has extensively been used to adjust stoichiometric growth conditions allowing severely reducing the surface roughness of layers and optimizing the hetero-interface and structural quality of multilayer stacks. The absence of polarization fields in cubic nitride nanostructures has been demonstrated. The performance of device structures taking advantage of this property like heterojunction field effect transistors (HFET) with both normally on and normally off characteristics as well as devices to demonstrate intersubband absorption in the spectral range between 1.55 μm and the terahertz region is summarized.

Keywords: cubic group III-nitrides, MBE, HRXRD, intersubband transitions, hetero field effect transistor

1. INTRODUCTION

Commercially available group III-nitride-based optoelectronic devices are grown along the polar c direction, which suffer from the existence of strong “built-in” piezoelectric and spontaneous polarization. This inherent polarization limits the performance of optoelectronic devices containing quantum well or quantum dot active regions. To get rid of this problem much attention has been focused on the growth of non- or semi-polar (Al,Ga,In)N. However, a direct way to eliminate polarization effects is the growth of cubic (100) oriented III-nitride layers. With cubic epilayers a direct transfer of the existing GaAs technology to cubic III-Nitrides will be possible and the fabrication of diverse optoelectronic devices will be facilitated. However, since cubic GaN is metastable and no cubic GaN bulk material exists in nature, heteroepitaxy with all its drawbacks due to lattice mismatch is necessary to grow this material. Due to the low lattice mismatch to cubic GaN the substrate of choice for the growth of cubic III-nitrides is 3C-SiC (001).

In this paper the latest achievements in the molecular beam epitaxy of phase-pure cubic GaN, AlN and their alloys grown on 3C-SiC (001) substrates are reviewed. A RHEED control technique is presented to carefully adjust stoichiometry and to severely reduce the surface roughness and hexagonal inclusions. The absence of polarization fields in cubic nitrides is demonstrated and 1.55 μm inter-subband absorption in cubic AlN/GaN superlattices is reported. The progress towards the

fabrication of cubic GaN/AlGaN superlattices for terahertz applications will be discussed and recent demonstrations of cubic III-nitride based heterojunction field effect transistors with both normally off and normally on characteristics will be shown.

2. MOLECULAR BEAM EPITAXY OF CUBIC III-NITRIDES

Cubic group III-nitride samples were grown on 200 μm thick, free standing 3C-SiC (001) substrates by molecular beam epitaxy (MBE) [1, 2]. An Oxford Applied Research HD25 radio frequency plasma source was used to provide activated nitrogen atoms. Aluminum and gallium were evaporated from Knudsen cells. Prior to growth, the 3C-SiC (001) substrates were chemically etched by organic solvents and a buffered oxide etch (BOE) and annealed for 10 hours at 500°C. Cubic GaN layers were deposited at 720°C directly on 3C-SiC substrates. The adsorption and desorption of metal (Ga, Al) layers on the c-GaN surface was investigated using the intensity of a reflected high energy electron beam (RHEED) as a probe. The structural and morphological properties of 3C-SiC substrates and group III-nitride epilayers were measured by high resolution X-ray diffraction (HRXRD) and atomic force microscopy (AFM). Reciprocal space mapping (RSM) has been performed to determine the Al molar fraction and the strain in the epilayers.

2.1 RHEED control

As an important step to improve the GaN surface morphology in a systematic way, it is essential to understand the surface structure and the underlying growth process on an atomic scale. In particular, the kinetic processes of adsorption and desorption on the surface are considered as key parameters that govern the surface morphology, incorporation kinetics and consecutively the overall material quality. In MBE of GaN, two dimensional surfaces are commonly achieved under Ga-rich conditions, with theoretical [3] and experimental [4, 5] evidence suggesting that the growth front is stabilized by a metallic Ga adlayers. The optimum conditions for the epitaxial growth of c-GaN are mainly determined by two parameters, the surface stoichiometry and the substrate temperature [1, 6]. Both parameters are interrelated; therefore an in-situ control of substrate temperature and surface stoichiometry is highly desirable. The study of the surface reconstruction by RHEED was one of the key issues in understanding the c-III nitride growth [1, 7, 8]. First principle calculations by Neugebauer et al. [9] show that all energetically favoured surface modifications of the non-polar (001) c-GaN surface are Ga-stabilized and therefore optimum growth conditions are expected under slightly Ga-rich conditions.

In Ref. 10 *in-situ* reflection high energy electron diffraction was used to quantitatively determine the Ga coverage of the GaN surface during growth. Figure 1 shows the RHEED intensity transient of the (0,0) reflection of the (2x2) reconstruction. After opening the Ga shutter we observe a steep linear decrease of the RHEED intensity between I_o and the kink position (I_k). The gradient of the intensity drop is related to the impinging Ga flux. Using the known value of the Ga flux and the time Δt_k it takes for the RHEED intensity to drop to I_k , we are able to calculate the amount of adsorbed gallium. Neglecting re-evaporation of Ga we get a total number of adsorbed Ga atoms from the flux time $\Delta t_k \times (I_o - I_k)$ product. In all cases this product is about $9.8 \times 10^{14} \text{ cm}^{-2}$, which is equal the number of atoms of exactly one monolayer

of Ga on the GaN surface (lattice constant of 4.52 \AA). Since I_0 is the reflectivity of the GaN surface and I_k is the reflectivity of GaN covered by one Ga monolayer, and the drop of the RHEED intensity in the time interval Δt_k is linear, the Ga coverage between 0 and one monolayer can be inferred from the measured intensity drop by linear interpolation. The decrease of the RHEED intensity below I_k is most likely due to further accumulation of Ga and thereby a modification of the Ga adlayer surface, however it is not proportional to the amount of adsorbed Ga. For this reason our method can only be used to measure the Ga coverage

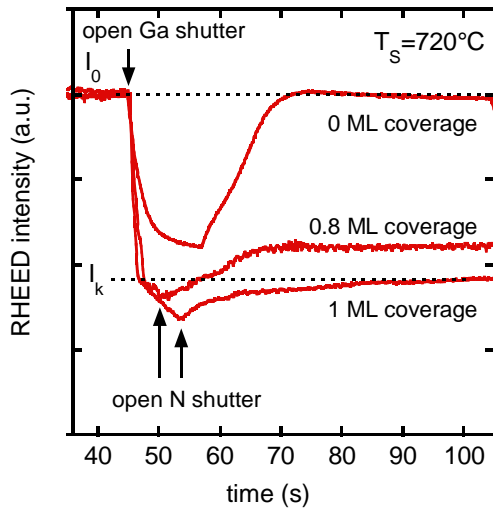


Figure 1: RHEED intensity transient measured during the growth of *c*-GaN, which started after opening the *N* source. The RHEED intensity measured during growth yields the amount of excess Ga (indicated in the figure) on the *c*-GaN surface. The Ga fluxes are 4.4×10^{14} , 3.2×10^{14} , and $1.2 \times 10^{14} \text{ cm}^{-2} \text{ s}^{-1}$ for the coverages of 1, 0.8, and 0 ML, respectively.

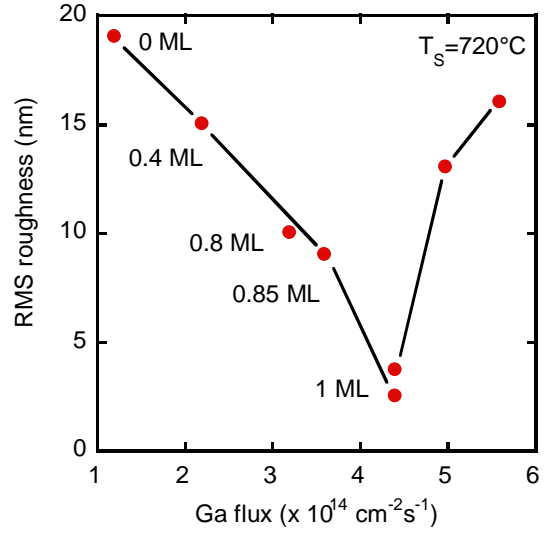


Figure 2: RMS roughness of *c*-GaN layers measured by $5 \times 5 \text{ \mu m}^2$ AFM scans vs Ga flux during growth. The corresponding values of the Ga coverage during growth are also included. Minimum roughness is obtained with an excess coverage of 1 ML. The line is a guide for the eyes

between zero and one monolayer, respectively. For Ga fluxes less than $3 \times 10^{14} \text{ cm}^{-2} \text{ s}^{-1}$ the situation is different. For these fluxes it is not possible to define a kink position. The RHEED intensity drops to a certain value and saturates. We suppose that then desorption of Ga cannot be further neglected. After opening the *N* shutter we observe an increase of the RHEED intensity which is due to the formation of *c*-GaN. During further growth the RHEED intensity saturates. From the saturation value the Ga coverage can be calculated using I_k as a reference. This procedure allows measuring the Ga-coverage in the range between 0 and 1 monolayer with an accuracy of 0.1 monolayers.

Figure 2 shows the root-mean-square (RMS) - roughness measured by a $5 \times 5 \mu\text{m}^2$ AFM-scan of several c-GaN layers versus the Ga flux used during MBE. The nitrogen flux was kept constant for all samples. The corresponding values of the Ga coverage during growth, as measured by the procedure described above, are included in Fig. 2. Only values below one monolayer can be measured. Minimum roughness is obtained with one monolayer Ga coverage during growth.

It has variously been suggested that excess Ga acts as surfactant during the epitaxy of hexagonal-GaN [11, 12, 13, 14]. The data shown in Fig. 2 clearly demonstrate that this effect exists also on the (001) surface of c-GaN. The width of the (002) X-ray rocking curve measured in double axis configuration of $1 \mu\text{m}$ thick c-GaN layers grown with one monolayer coverage is about 16 arcmin. Among our c-GaN layers with equal thickness 16 arcmin is a minimum value. Gallium fluxes which are equivalent to a Ga coverage exceeding one monolayer lead to a pronounced increase of the roughness and the FWHM of the X-ray rocking curve.

2.2 Cubic GaN

High-resolution X-ray diffraction (HRXRD) enables to measure the density of extended defects in epitaxial layers. The full width at half maximum (FWHM) of the Bragg reflex obtained in a direction perpendicular to the diffraction vector (ω -scan) is related to the intensity of extended defects in the layer. The ω -scan measures the intensity spread for the coordinate q_{\perp} in reciprocal space arising from both mosaicity and finite lateral domain size. Fig. 3 compiles HRXRD data from c-GaN layers with a varying thickness grown by MBE on GaAs [15, 16] and 3C-SiC [17] substrates, respectively. A clear decrease of the FWHM with increasing layer thickness is seen and the values given in Reference [16] are quite comparable to our data. The linewidths measured for c-GaN grown on 3C-SiC substrates are approximately a factor of three narrower than that for layers grown on GaAs substrates. This may be expected due to the lower lattice mismatch of this system. The clear trend of decreasing FWHM with increasing layer thickness immediately implies that the number of extended defects is reduced in thicker epilayers.

In Fig. 3 the rocking curve line width (ω -scan) of all cubic GaN epilayers (full triangles) grown on 3C-SiC is plotted versus c-GaN layer thickness. Two effects can clearly be seen from this plot. First a severe reduction of the full width at half maximum (FWHM) with increasing epilayer thickness is observed. This linewidth dependence is consistent with the defect annihilation process observed in cubic GaN grown on GaAs (001) substrates [18]. Since in zinc-blende structure the stacking faults (SFs) lie on the (111) planes, an annihilation mechanism is possible, when two SFs, lying, for example on the (111) and on the (-1-11) planes intersect and annihilate simultaneously with the creation of a sessile dislocation aligned along [110] directions. For the case of 3C-SiC, where the lattice mismatch is only -3.7% to cubic GaN, the full line shows the theoretical calculated FWHM as a function of layer thickness using the dislocation glide model by Ayers [19]. This model implies that the dislocation density N_{disl} is inversely proportional to the layer thickness d and that the FWHM is proportional to $d^{-1/2}$. In addition with this model order of magnitude accuracy in quantitative predictions of the dislocation densities for a number of heteroepitaxial systems can be achieved. The full line through the 3C-SiC data shows this model calculation, which gives a relation between the dislocation density N_{disl} , the lattice misfit

between substrate and epitaxial layer and the thickness of the epilayer. In the calculation it was assumed that 60° dislocations with a Burgers vector of 0.32 nm are the predominant defects in the layers. The trend of the calculated curve is in excellent agreement with the experimental data. The estimated dislocation density N_{disl} is shown on the right hand scale of the diagram. Comparing the full curve with the experimental data (full triangles) a reduction of the FWHM by a

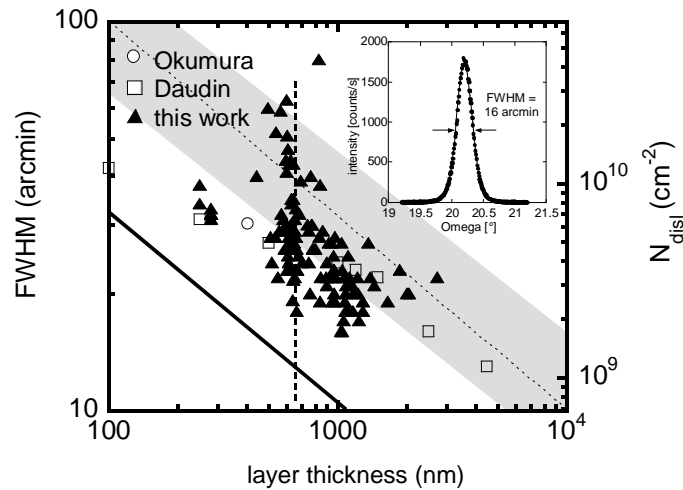


Figure 3: Rocking curve linewidth of cubic GaN epilayers grown on 3C-SiC substrates versus thickness of the cubic epilayers.

factor of 1.5 is still possible. By comparing these data with data cited in literature the dependence of the FWHM on film thickness has to be taken into account. Up to now, only two other groups reported data on GaN on 3 - 5 μm thick 3C-SiC/Si (001) pseudo-substrates grown by chemical vapor deposition (open circle Ref. [20] and open squares Ref. [17]). As can be seen in Fig.3 we clearly are able to remain under the best cited values, indicating the improved structural quality of our c-GaN epilayers due to the availability of free standing, bulk like 3C-SiC (001) substrates. The HRXRD data are in good agreement with TEM investigations [16] which yield a defect density in the order of 10^9 to 10^{11}cm^{-2} . In addition, TEM measurements further showed that the density of stacking faults is drastically decreasing with increasing layer thickness. As mentioned above, the second parameter which strongly influences the quality of the cubic epilayers is the roughness of the 3C-SiC substrate. In Fig. 3 the linewidth of the rocking curve of 600 nm thick cubic GaN epilayers on 3C-SiC substrates varies from 60 arcsec to 20 arcsec for substrates with different surface roughness (indicated by the vertical dashed line). The root mean square (RMS) roughness of the corresponding 3C-SiC substrates as measured by AFM on $5 \times 5 \mu\text{m}^2$ large areas varied between 11 nm and 0.7 nm, respectively. The smoother the surface of the substrates the narrower is the FWHM and the higher is the structural quality of the cubic epilayer. This observation is in agreement with measurements of Ref. [20] and indicates that a further improvement of the surface preparation (atomic

flat surfaces) may allow to achieve the theoretical limit indicated by the full line. Up to now, the X-ray rocking curve of a 1 μm thick c-GaN layer grown with 1 monolayer coverage was about 16 arcmin (see inset of Fig. 3), which is one of the best values reported so far.

For the sake of completeness the shaded area in Fig. 3 depicts the range of FWHM values as measured for cubic GaN grown on GaAs substrates. However, the model of Ayers cannot be applied to heteroepitaxial systems with mismatch greater than about 10 % since in such systems the misfit dislocations are so closely spaced that the continuum elasticity theory cannot predict their line tension with acceptable accuracy. However, if we shift the calculated line upwards, one sees that for the c-GaN/GaAs case the same trend is observed (dashed line through shaded area). Therefore the the same defect annihilation process is also effective in the GaAs case. From the right hand scale we estimated a dislocation density of about 10^{10} cm^{-2} for a 1 μm thick c-GaN epilayer on GaAs (001).

From experiments it is well known that hexagonal inclusions mainly grow on (111) facets and cannot be detected by ω - 2θ -scans. Therefore reciprocal space maps (RSM) of the GaN (002) Bragg-reflection were performed. The RSM of a 600 nm thick cubic GaN epilayer on 3C-SiC substrate along the (-110) azimuth is shown in Fig. 4. Only a very weak intensities of the (10-11) and (-1011) reflections from hexagonal GaN (indicated in Figure 4 by arrows) is measured yielding a content of hexagonal inclusions below 1%.

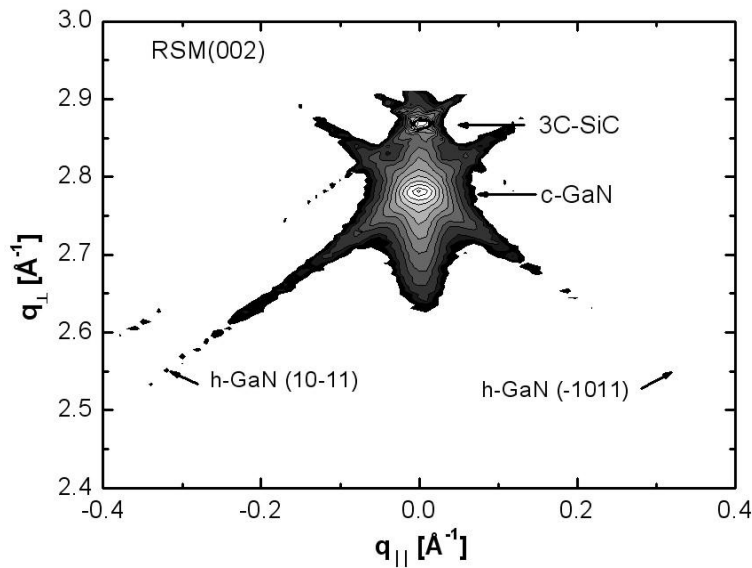


Figure 4: Reciprocal space map of a 600 nm thick cubic GaN epilayer grown on 3C-SiC substrates. High intensity (002) Bragg reflections of c-GaN and the 3C-SiC substrate are observed. Only a very weak (10-11) reflection from hexagonal GaN is measured yielding a content of hexagonal inclusions below 1 %.

2.3 Cubic AlN

AlN is a wide-band gap semiconductor with a large thermal conductivity comparable to copper, a hardness close to sapphire and a high chemical stability. Until recently the meta-stable cubic phase of AlN had a considerable surface roughness, leading to short-circuits and broadening of confined electronic states of low dimensional structures [21,22]. However, the PAMBE growth of atomically flat c-AlN layers on freestanding 3C-SiC substrate was reported recently [23]. The growth procedure started with a deoxidation of the substrate. Surface oxides lead to blurred reflections of the cubic lattice, three dimensional islands on the surface cause disc shape reflections due to an electron transmission component [24]. After cleaning the RHEED pattern of the 3C-SiC surface shows long thin streaks indicating a two dimensional oxide free surface with a (2x4) reconstruction and Kikutchi lines. The used cleaning process can be found in more details in Ref. 23.

Exposing an c-AlN surface to nitrogen leads to the formation of hexagonal clusters. However, growing c-AlN with one monolayer Al surface coverage can prevent hexagonal condensation [23, 25]. Therefore, the c-AlN nucleation on the 3C-SiC substrate was done under one monolayer (ML) of Al surface coverage. The substrate temperature was 730°C and the Al beam flux was $2 \cdot 10^{14} \text{ cm}^{-2} \text{ s}^{-1}$, respectively. The growth was monitored *in-situ* by RHEED. At the initial growth process a transition from 2D to a 3D surface was observed. This transition is clearly seen in Fig. 5 where the RHEED pattern after the deposition of 6 ML of c-AlN (Fig. 5 (a)) is compared with that after deposition of 30 ML (Fig. 5 (b)). The spotty reflections originating from an electron transmission component through islands on the surface are transformed into long streaks. After a smooth surface was established, growth interruptions of 30 seconds were applied every 20 atomic layers to avoid metal accumulation at the surface. RHEED intensity oscillations (not shown here) indicate a two-dimensional layer-by-layer growth and the growth rate was determined to be 0.2 ML/s. A smooth 2D surface is still seen after the growth of 142 nm (650 ML) c-AlN (see RHEED pattern in Fig. 5 (c)).

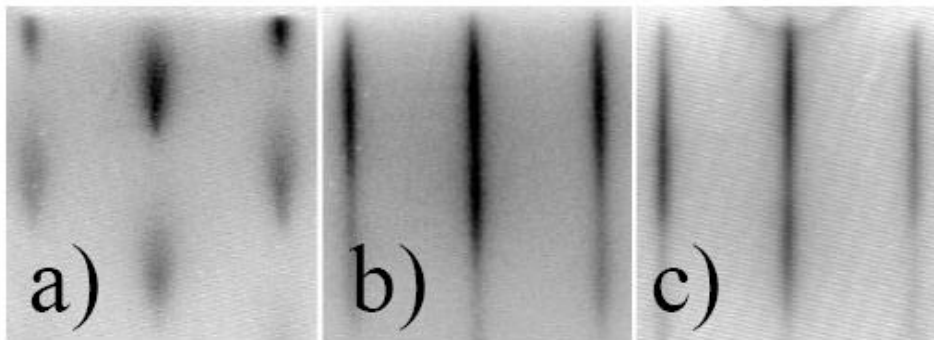


Figure 5: RHEED images of the c-AlN surface during the initial growth process. (a) after growth of 6 ML, (b) after growth of 30 ML, (c) after growth of 650 ML.

The cubic structure of the AlN layer is clearly shown by HRXRD measurements. In Fig. 6 the HRXRD (113) reciprocal space map of a 300 nm c-AlN layer on 3C-SiC is shown. The peak of the arrow 3 indicates the position of the 3C-SiC

Bragg reflection, the peak of arrow 1 indicates the position of the c-AlN reflection. The elliptic shape originates from a mosaic structure caused by strain relaxation [26]. The main axis of the ellipse (white line in Fig. 6 labelled by 4) is perpendicular to the reciprocal lattice vector. A small shift of the c-AlN peak along the main axis can be interpreted as tilt of the c-AlN layer versus the substrate. Taking this tilt into account the position of the c-AlN reflection is shifted to the peak position indicated by arrow 2. The c-AlN lattice parameter in growth direction extracted from Fig. 6 is $4.373 \text{ \AA} \pm 0.002 \text{ \AA}$.

The high surface quality of the c-AlN layers is verified with AFM. The AFM image of the c-AlN layer shows an atomically smooth surface with a roughness of 0.2 nm RMS. The according line scan depicts a peak-to-valley height of only 1 lattice constant over a lateral extension of ~ 2000 lattice constants.

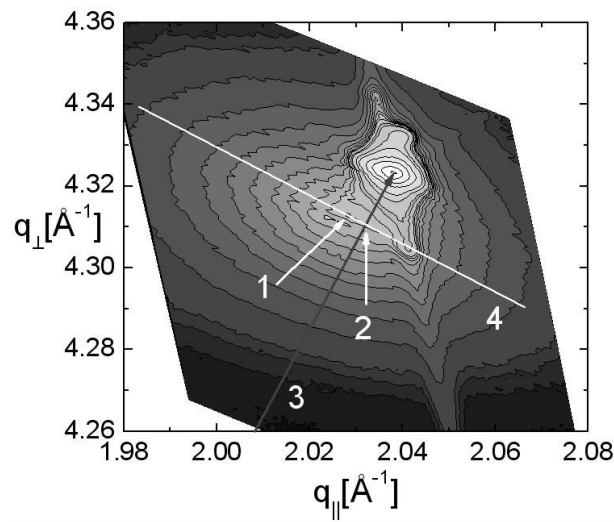


Figure 6: HRXRD reciprocal space map of the (113) reflections of c-AlN and 3C-SiC. (1) position of the c-AlN peak, (2) position of c-AlN peak after tilt correction, (3) reciprocal lattice vector of 3C-SiC reflection, (4) axis for tilt correction perpendicular to (3).

A commercial ellipsometer was employed for recording the ellipsometric parameters Ψ and Δ under different angles of incidence (Φ : 60° , 67° , and 74°) in the photon ($\hbar\omega$) energy range from 1 to 6.4 eV. A home-made construction attached to the Berlin Electron Storage Ring for Synchrotron Radiation (BESSY II) allowed measurements of Ψ and Δ under $\Phi=67.5^\circ$ from 5 to 10 eV with the set-up described in Ref. 27. The dielectric function (DF) was obtained by a multi-layer fitting procedure similar to the approach presented in Ref. 28. No assumption was made concerning the shape of the DF, i.e. the real (ϵ_1) and imaginary parts (ϵ_2) of the DF were separately fitted for all photon energies. Figures 7 a) and b) summarize the results of the fitting procedure for one of the cubic AlN films (layer thickness here was 100 nm). The spectral dependence shows similarities to the recently reported results for the hexagonal counterpart [29] however, the characteristic energies E_0 , E_1 , and E_2 differ appreciably.

The imaginary part of the DF exhibits a sharp onset at 5.88 eV which defines the direct excitonic band gap. Adopting the exciton binding energy of 50 meV for the hexagonal AlN [30] the direct band gap (E_0) is determined at the Γ point of the Brillouin zone with 5.93 eV. This result is in excellent agreement to the calculated quasi-particle band gap of 5.86 eV if the lattice polarizability is taken into account [30]. For comparison, previous studies of mixed phase AlN yielded 5.74 eV for the zinc-blende compound [31]. The pronounced absorption tail below 5.88 eV in Fig. 7 b) is attributed to phonon-assisted indirect absorption. The imaginary part differs appreciably from zero only above 5.3 eV, i.e. this energy defines the upper limit of the indirect band gap. A slightly lower value might be possible as well, but ellipsometry is not sensitive enough in the case of low absorption. Finally, the E_1 and E_2 transition energies at room temperature amount to 7.20 and 7.95 eV, respectively.

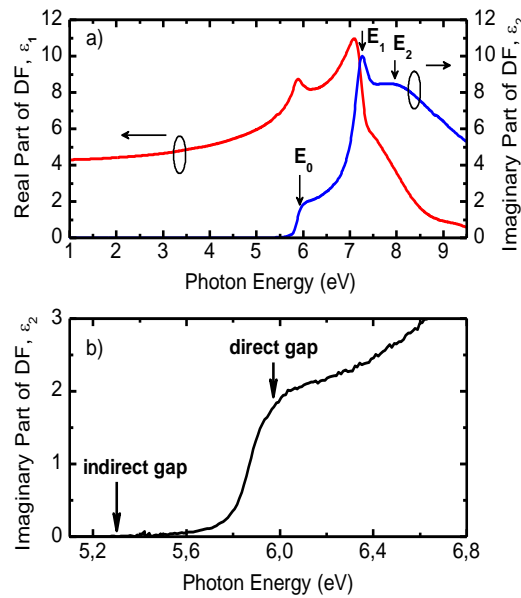


Figure 7: a) Real and imaginary part of the DF for c-AlN from 1 to 10 eV. b) Magnification of the region close to the absorption edge.

2.4 Cubic AlGa_xN/GaN Quantum Wells

Cubic Al_xGa_{1-x}N epilayers and cubic Al_xGa_{1-x}N/GaN MQW have been grown by MBE at 720°C. Such Al containing epilayers are necessary for cladding layers in laser diodes or LEDs and are also used in resonant cavity LEDs for the realization of Al_xGa_{1-x}N/GaN distributed Bragg reflectors.

Figure 8 shows the XRD ω -2 θ scan of the (002) Bragg-reflection of a 15 period Al_xGa_{1-x}N/GaN MQW structure (upper curve). The reflections of the 3C-SiC substrate, of the c-GaN buffer as well as several superlattice peaks (SL-5 to SL+2) are clearly seen. This indicates a good Al_xGa_{1-x}N/GaN interface quality. The experimental data have been fitted using dynamic scattering theory (lower curve), yielding a well width of 10.2 nm, a barrier width of 10.8 nm and an Al mole fraction of $x=0.3$. These values are in excellent agreement with data, which were obtained from growth rate

measurements using RHEED oscillation period. The appearance of RHEED oscillations after opening the Al shutter [24] emphasizes a two dimensional $\text{Al}_x\text{Ga}_{1-x}\text{N}$ growth mode at substrate temperatures of 720°C .

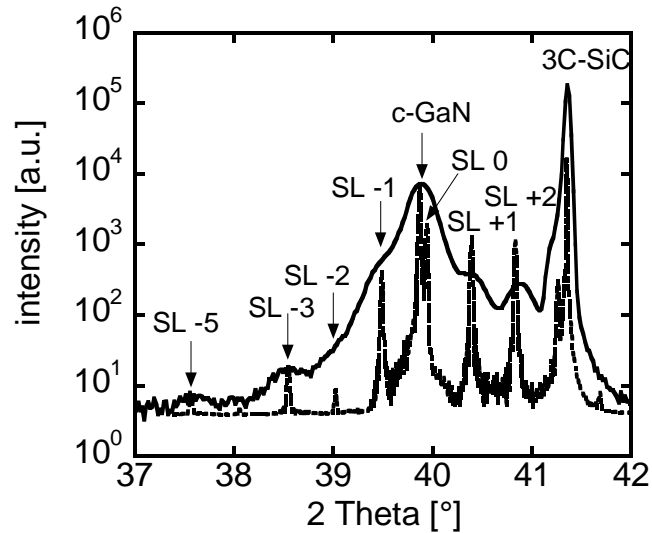


Figure 8: Measured $\omega-2\theta$ scan of $15 \times \text{Al}_{0.3}\text{Ga}_{0.7}\text{N}/\text{GaN}$ MQW structure (solid line) and simulated data (dotted line).

The well and the barrier width are 10.2 nm and 10.8 nm, respectively.

To demonstrate the absence of internal spontaneous polarization fields in cubic group III-nitrides cubic single and multi $\text{Al}_{0.15}\text{Ga}_{0.85}\text{N}/\text{GaN}$ quantum wells were grown on 3C-SiC/GaN substrates [32]. The quantum structures consist of 6 nm thick $\text{Al}_{0.15}\text{Ga}_{0.85}\text{N}$ barriers and GaN wells with a width of 2.5 –7.5 nm and were sandwiched between 50 nm AlGaN cladding layers. During growth of $\text{Al}_{0.15}\text{Ga}_{0.85}\text{N}/\text{GaN}$ QWs clear RHEED oscillations were observed allowing a stringent control of the growth rate and indicating two dimensional growth of the respective layers. The room temperature photoluminescence spectra of a multi quantum well (MQW) structure excited with a HeCd-UV laser is shown in the inset of Figure 9. The dimensions of the quantum structures are 3 nm thick wells and 6 nm barriers. A strong emission is observed at 3.30 eV, which lies between the c-GaN emission at 3.2 eV and the emission of the $\text{Al}_{0.15}\text{Ga}_{0.85}\text{N}$ cladding layer at about 3.48 eV [33]. The PL linewidth of cubic QW luminescence is about 103 meV and is almost comparable to values reported for non-polar hexagonal AlGaN/GaN quantum wells [34]. The slightly broader linewidth in the cubic structures is attributed to the higher density of dislocations.

Figure 9 depicts the dependency of the QW emission energy on the well width for both cubic (blue squares) and hexagonal QWs (red dots). Therein, the shift in transition energies compared to the band gap energy is plotted versus well width. For our cubic $\text{Al}_{0.15}\text{Ga}_{0.85}\text{N}/\text{GaN}$ QWs the peak energy of the emission exactly follows the square-well Poisson-Schrödinger model and demonstrates the absence of polarization induced electrical fields. For comparable hexagonal $\text{Al}_{0.17}\text{Ga}_{0.83}\text{N}/\text{GaN}$ QWs on sapphire substrates the experimental data can only be explained if an internal spontaneous electrical field of 750 kV/cm is taken into account [35]. These results indicate that the well known thermodynamic metastability of the cubic nitrides does not necessarily limit their application for polarization free structures.

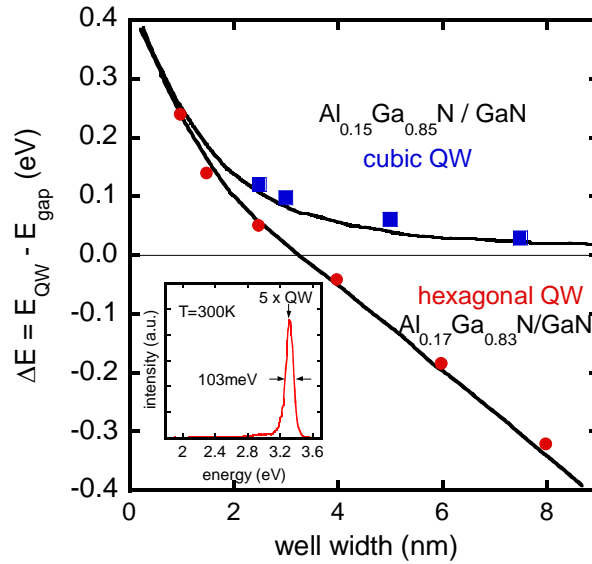


Figure 9: Transition energies of $\text{Al}_{0.15}\text{Ga}_{0.85}\text{N}/\text{GaN}$ MQWs versus well width for cubic (blue squares) and hexagonal (red dots) MQWs. The squares and dots are experimental data; the curves are calculated using a self-consistent Poisson-Schrödinger model. For the hexagonal QWs an internal field of 750 kV/cm is estimated. Inset: Room temperature photoluminescence spectrum of a cubic MQW.

3. DEVICE APPLICATIONS OF CUBIC III-NITRIDES

The group III-nitrides became the well established material basis for a number of optoelectronic and electronic devices. The thermodynamically stable, hexagonal phase of these semiconductors is predominantly grown on the c-plane surface of sapphire or SiC, which as a consequence of the crystal symmetry leads to the inherent formation of spontaneous and piezoelectric polarization fields which can be detrimental for some device applications, (e.g. multi quantum wells for terahertz emitters.) Therefore growth of so-called non-polar and semi-polar structures has attracted growing interest in the last years. This may be done by using a- or m-plane substrates for the preparation of hexagonal III-nitrides or to grow cubic-phase III-nitrides which may be considered as the real non-polar modification of this class of materials. In the following recent activities to realize various device concepts which take advantage of the absence of polarization fields are summarized.

3.1 Cubic AlN/GaN quantum wells for Intersubband spectroscopy

Progress in hexagonal III-nitride epitaxial growth has extended the optoelectronic applications of this material system from the ultraviolet region to the near infrared spectral region. [36-42]. The ability to engineer quantum well structures consisting of $\text{Al}_{1-x}\text{Ga}_x\text{N}$ and GaN over a wide spectral range was made possible by the considerable conduction band offset between the two binaries AlN and GaN (~ 1.8 eV). [42] It is the magnitude of this band offset that theoretically

enables the tuning of intersubband (ISB) transition wavelengths towards the technologically important wavelengths such as 1.55 μm . Great strides in understanding the growth kinetics of hexagonal nitride materials has enabled steady progress in the growth and fabrication of detectors based on the intersubband transitions in GaN/AlN-based systems [37-39,43,44]. However, the large built-in electrostatic fields in polar hexagonal heterostructures grown on c-plane (0001) sapphire strongly influence their optical and electrical properties [45, 46]. Efforts to circumvent these effects have been accomplished using R-plane ($10\bar{1}2$) sapphire substrates which result in non-polar *a*-plane ($11\bar{2}0$) hexagonal nitride material, thus effectively eliminating the contributions of these polarization fields [47, 48].

On the other hand, spontaneous polarization and piezoelectric fields do not exist in cubic GaN/AlN heterostructures and quantum wells. Thus, it was of interest to investigate the intersubband transitions in this particular cubic GaN/AlN quantum structure. The optical absorption due to the intersubband transition in non-polar cubic GaN/AlN short period superlattices grown by plasma assisted MBE on 3C-SiC substrates has first been reported by E.A. DeCuir et al. [49]. All quantum structures were grown at 720 $^{\circ}\text{C}$ on free standing 3C-SiC (001) substrates by plasma assisted molecular beam epitaxy. A 100 nm thick c-GaN buffer was deposited on a 3C-SiC substrate using the RHEED control of the growth process [10]. Subsequently, a 20 period GaN/AlN superlattice (SL) was grown. The barrier thickness was fixed at 1.35 nm for all samples while the well thickness was varied in the range between 1.6 and 2.1 nm. Finally, the quantum structures were capped with a 100 nm thick c-GaN layer. To increase the optical absorption length, the samples were cut into waveguide geometry to allow for multiple passes. Intersubband transitions were then observed in absorption spectra in the range of 1.5 to 2 μm . The experimental results are summarized in Table I. They are found to be in good agreement with peak energies calculated as a function of the well width using a propagation matrix method. Good agreement was obtained between the calculated and measured values [49].

Sample number	Superlattice period (nm)	L_w (nm)	E_{peak} (meV)		FWHM (meV)	n_{2D} (10^{11} cm^{-2})	E_F (meV)
			Measured	Calculated			
A	3.45	2.1	620	630	182	2.79	3.52
B	3.1	1.75	696	734	211	2.33	2.94
C	2.95	1.6	751	781	219	2.13	2.68

Table I: Summary of the 20-period cubic-GaN/AlN superlattice samples used in the present study. The period is obtained from the high resolution x-ray diffraction, L_w (nm) is the well width, E_{peak} is the peak position energy obtained from the experimental measurements, FWHM is the full width at half maximum of the intersubband transition spectra, n_{2D} is the two dimensional electron gas obtained by electrochemical capacitance measurements, and E_F is the Fermi energy level [49].

The intersubband absorption of cubic GaN/Al(Ga)N QW superlattices in a wider spectral range was reported by M. Machhadani et al. [50]. By varying the QW thickness and Al content it was possible to tune the ISB absorption wavelength from 1.4 μm to even 63 μm (~ 4.8 THz). This corresponds to the shortest and the longest ISB wavelength ever achieved with this material system.

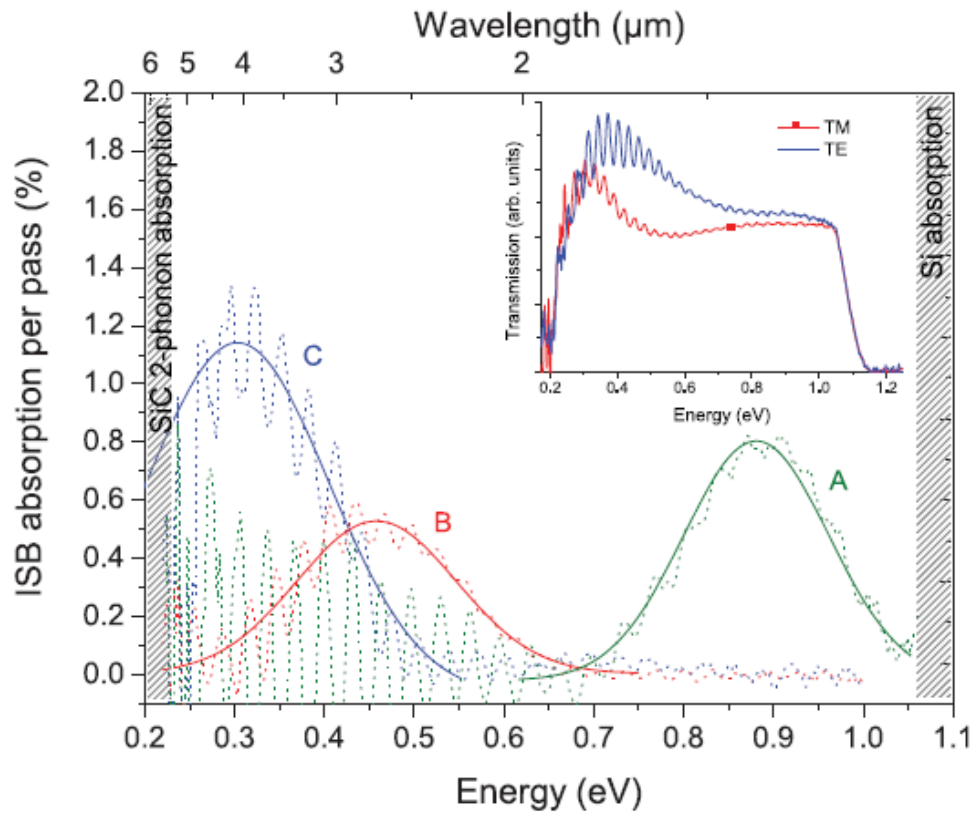


Figure 10: Room-temperature TM absorption (characteristic of ISB transitions) per pass in the active region of three samples A, B, and C (dotted curves) and corresponding Gaussian fits (full curves). Inset: Room-temperature infrared transmission spectrum of sample B for TM- and TE-polarized light.

A typical transmission spectrum for TM-(p-) and TE-(s-) polarized light is shown in the inset of Fig. 10. The spectrum is normalized by the response of the optical system. The oscillations observed in the spectrum arise from the Fabry-Perot interferences in the 10 μm thick SiC layer. The high energy cut-off corresponds to the absorption of the Si substrate whereas the low energy transmission drop at 0.21 eV corresponds to the two-phonon absorption of the SiC template. An absorption peak at 0.46 eV is observed for TM-polarized light which is a clear signature of an ISB resonance.

Figure 10 displays the ISB absorption spectra of three different samples together with the corresponding Gaussian fits. The absorption peaks are at 1.4 μm (sample A), 2.7 μm (sample B), and 4.1 μm (sample C), respectively. These data show that the broadening of the ISB absorption in cubic QWs is larger than in their hexagonal counterparts. For example, the full width at half maximum (FWHM) is 0.17 eV which is slightly higher than the typical broadening observed for

hexagonal GaN/AlN QWs absorbing in the same spectral range (typically 60-100 meV in doped QWs [51, 52] and 40 meV in undoped samples [53]. In Ref. [54] the broadening is attributed to thickness fluctuations, interface roughness and impurity scattering as in the case of GaAs/AlGaAs QWs. The large broadening in relatively wide cubic QWs may be due to fluctuations of the QW thickness which have a stronger influence on the transition energy in the case of cubic QW than in hexagonal QW, because internal electric fields in the latter confine the carriers and makes the transition energy almost thickness-independent [55].

The quantum confinement in cubic QWs was modeled using an effective mass model. The PL and ISB transition energies of the QW structures were then calculated by self-consistently solving the Schrödinger and Poisson equations. These simulations allowed to obtain some material parameters, e.g. the electron effective mass in cubic GaN was estimated to be close to $0.11m_0$ and the CB offset between GaN and AlN was found to be about 1.2 eV or higher. The valence-band offset (VBO) and the conduction band offset (CBO) were also calculated using an ab-initio approach (calculating many-body corrections) within the *GW* approximation on top of hybrid-functional density functional theory calculations. A CBO of (1.4 ± 0.1) eV and a VBO of (0.5 ± 0.1) eV is obtained in good agreement with the values deduced from measured intersubband transition energies [56].

The transmission measurements in the THz spectral region were performed at 4.7 K in a Bruker Fourier transform infrared spectrometer using a glow-bar source and a liquid helium-cooled Si bolometer. The sample was cut into two pieces of same length. Both pieces were polished with 30° facets and placed face to face under mechanical pressure on the cold finger of a liquid helium-cooled cryostat. This configuration allowed enhancing the light transmission by doubling the surface of the input facet. Placing the active QWs face to face also provides a good coupling of the TM-polarized THz radiation with the ISB transitions.

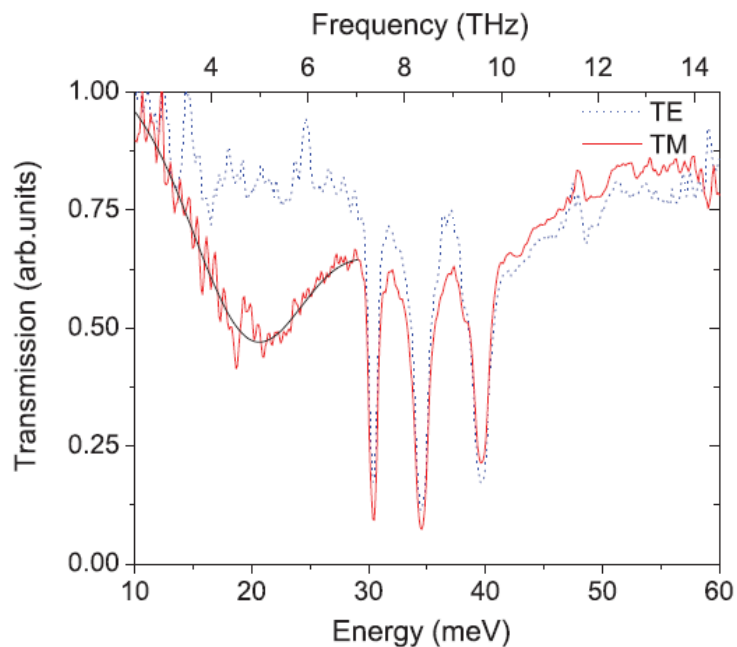


Figure 11: Low-temperature far-infrared transmission spectrum of an $\text{Al}_{0.05}\text{Ga}_{0.95}\text{N}/\text{GaN}$ MQW structure for TM-polarized light (red solid line) and TE-polarized light (blue dotted line). The black solid line is a Gaussian fit of the absorption with a linear baseline.

Figure 11 shows the transmission spectrum of an $\text{Al}_{0.05}\text{Ga}_{0.95}\text{N}/\text{GaN}$ MQW structure for TM- and TE-polarized light [50]. The transmission of the sample has been normalized to 1 at low energies. As seen in Fig. 11, the sample exhibits absorption peaked at 19.7 meV (4.76 THz) only for TM-polarized light, which is a clear signature of ISB absorption. The three absorption resonances between 30 and 40 meV which are not influenced by the light polarization are related to the SiC-on-Si substrate.

These first observations of ISB absorption at THz frequencies in cubic $\text{GaN}/\text{Al}_{0.05}\text{Ga}_{0.95}\text{N}$ QWs may open prospects for the future development of quantum cascade lasers operating at non-cryogenic temperature in this material system.

3.2 Cubic AlGaN/GaN heterojunction field effect transistors

Beside the impressive application of group III nitrides in optoelectronics the number of electronic devices based on wide gap III-nitrides is presently increasing. Due to the large bandgap of GaN and AlN and their ternary compounds they are good candidates for high frequency and high power devices and tremendous research activities have been undertaken to grow multilayer group III-nitride stacks in still improving crystalline perfection. Most of these activities have been devoted to group III-nitrides with wurtzite (hexagonal) crystal structure.

However, group III-nitrides can also be grown in the less energetically favorable cubic (zincblende) structure, which due to the absence of built-in electric fields have some potential advantages over their hexagonal counterparts where built-in electric fields arising from spontaneous and piezoelectric polarization may set limits to the performance of some electronic devices. Thus the cubic structure may be advantageous for some device applications like normally-off field effect transistors. Also phonon scattering is lower in the cubic phase due to the higher crystallographic symmetry. As a result the mobility of electrons and holes in the cubic phase is expected to be larger than in hexagonal structures.

AlGaN/GaN hetero-junction field-effect transistors (HFETs) are of interest for high-power and high-frequency amplifiers. This is motivated by their potential in commercial and military applications, e. g. in communication systems, radar, wireless stations, high-temperature electronics and high-power solid-state switching. Currently, state of the art HFETs are fabricated on *c*-plane wurtzite AlGaN/GaN heterostructures. Their inherent polarization fields produce extraordinary large sheet carrier concentrations at the AlGaN/GaN hetero-interface which are advantageous for normally-on type transistors [57-59].

However, for switching devices and digital electronics field-effect transistors (FETs) with normally-off characteristics are desirable. It was discussed by Abe et al. [60] that the use of cubic III-nitrides would offer fabricating HFETs without parasitic polarization fields and with equal electrical properties for all gate orientations. Further, with cubic nitrides the same technology for the production of normally-on and normally-off devices can be applied. A first demonstration of a *c*-nitride HFET with normally-off characteristics with a threshold voltage of $V_{th}=0.6$ V has recently been reported by E. Tschumak et al. [61].

For the epitaxy of cubic AlGaN/GaN hetero structures freestanding Ar^+ implanted 3C-SiC (001) substrates were used. A three energy implantation with Ar^+ ions at doses of $6 \times 10^{14} \text{ cm}^{-2}$ at 160 keV, $2.4 \times 10^{14} \text{ cm}^{-2}$ at 80 keV and $1.2 \times 10^{14} \text{ cm}^{-2}$ at 40 keV was applied to form an isolating damage layer near the surface. The *c*-AlGaN/GaN layer stacks consist of 200 nm unintentionally doped (UID) cubic GaN (*c*-GaN) followed by 4 nm UID cubic $\text{Al}_{0.33}\text{Ga}_{0.67}\text{N}$ (*c*- $\text{Al}_{0.33}\text{Ga}_{0.67}\text{N}$)

spacer layer, 6 nm thick c-Al_{0.33}Ga_{0.67}N doped with $N_D=4\times 10^{18}$ cm⁻³ Si and 10 nm UID c-Al_{0.33}Ga_{0.67}N. The root-mean square (RMS) roughness of the c-Al_{0.33}Ga_{0.67}N surface measured by atomic force microscopy was 3 nm. The dislocation density of c-GaN was about 5×10^9 cm⁻² as estimated from the full-width at half maximum (FWHM) of the x-ray rocking curve of the (002) c-GaN reflex. Thus the crystalline properties of the c-AlGaN/GaN hetero-structures were comparable with those of hexagonal a-plane structures [62].

Ti/Al/Ni/Au (15 nm/50 nm/15 nm/50 nm) was thermally evaporated and annealed at 850 °C for 30 s in nitrogen atmosphere to form source and drain contacts with ohmic characteristics. Then, c-AlGaN/GaN mesas were formed by SiCl₄ reactive ion etching (RIE) in order to separate single devices. Gate fingers were fabricated by evaporation of Pd/Ni/Au (15 nm/15 nm/50 nm) and subsequent annealing at 400 °C for 10 min. The devices had a gate length of 2 μm, a gate width of 25 μm and a source-to-drain spacing of 8 μm. Finally contact pads were thermally evaporated onto a 250 nm thick SiO₂ layer which was deposited around the FET devices for isolation.

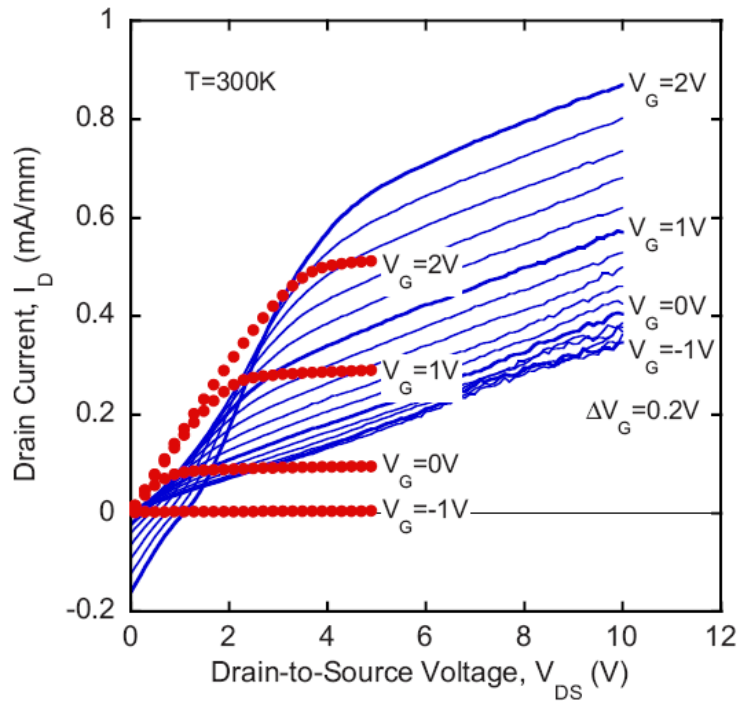


Figure 12: Static output characteristics of a fabricated cubic AlGaN/GaN HFET. The dotted lines represent calculated output characteristics at $V_G=-1, 0, +1,$ and $+2$ V.

Figure 12 shows the room temperature DC drain current-voltage (IV) curves of a c-HFET revealing a clear field-effect when the gate-to-source voltage is varied from -1V to +2V. A parasitic shunt current $I_{shunt}=0.34$ mA/mm was observed at $V_{DS}=10$ V. Most likely It is caused insufficient isolation between the device and the high conductive 3C-SiC substrate. The source-to-drain current difference between $V_G=-1$ V and $V_G=+2$ V was 0.5 mA/mm which is 20 times lower than the source-to-drain current of *a*-plane AlGaN/GaN HFET with a [1-100] gate orientation [62]. It was

suggested in [61] that this difference is mainly due to the relatively high resistivity of the source and drain contacts of $\rho_C=150 \Omega\cdot\text{cm}$ which have not yet been optimized.

From the gate contact I-V characteristics shown in Fig. 13 it was concluded that (i) the negative drain current at $V_{DS}=0 \text{ V}$ and $V_G > 1 \text{ V}$ is caused by gate leakage in forward direction and (ii) the drain current of 0.34 mA/mm at $V_{DS}=10 \text{ V}$ and $V_G=0 \text{ V}$ is mainly due to reverse gate leakage ($I_G=0.3 \text{ mA/mm}$ at $V_{DS}=10 \text{ V}$ and $V_G=0\text{V}$).

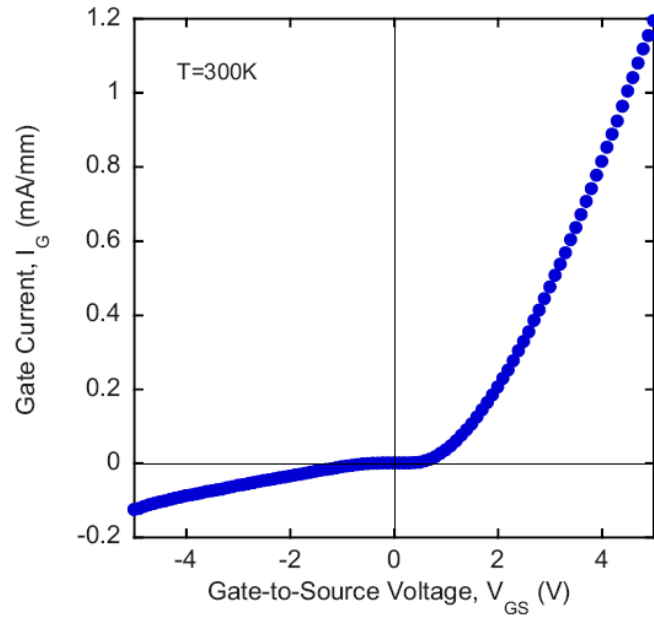


Fig. 13: Room temperature I-V characteristics of the gate contact.

From the output characteristics the field-dependent electron mobility at the c-AlGa_{0.33}N/GaN interface was estimated. It is slightly smaller than the Hall mobility of *a*-plane AlGa_{0.33}N/GaN FETs where a maximum mobility of $46 \text{ cm}^2/\text{Vs}$ was measured [62].

The output characteristics of these first cubic HFET devices were calculated using the two-dimensional device simulator ATLAS [63]. The parameters used in the simulation were a 3C-SiC substrate with zero conductivity followed by 200 nm c-GaN buffer layer, a 4 nm c-Al_{0.33}Ga_{0.67}N spacer layer with $N_D=4*10^{17} \text{ cm}^{-3}$, a 6 nm layer with $N_D=4*10^{18} \text{ cm}^{-3}$, and a 10 nm cap layer with $N_D=4*10^{17} \text{ cm}^{-3}$. A donor concentration of $N_D=4 *10^{16} \text{ cm}^{-3}$ and an electron mobility of $5 \text{ cm}^2/\text{Vs}$ at the c-AlGa_{0.33}N/GaN interface was assumed. Further a linear decrease in the donor concentration and mobility with increasing distance from the surface had to be taken into account to fit best the experimental data. This assumption seems reasonable since it has been shown in Ref. 64 that the dislocation density of c-GaN layers increases with decreasing distance to the substrate-layer interface. The contact resistivity of the source and drain contacts was set to $\rho_C=150 \Omega\text{cm}$. The Schottky gate contact with a barrier height of 0.8 eV was localized on top of the c-AlGa_{0.33}N layer. Like in the realized HFET devices the gate length was $2 \mu\text{m}$ and the gate-to-source and gate-to-drain spacing was $3 \mu\text{m}$. Unfortunately, it was not possible to include the effect of gate leakage in the simulation. The dotted lines in Fig. 12 represent the calculated drain current I_D of the HFET at $V_G=-1 \text{ V}$, 0 V , 1 V , and 2 V , respectively. The increase in the calculated drain

current with increasing V_G is in good agreement with the measured data. However, experimental data show a drain current at $V_G=0V$ which is not found in the simulation. It was concluded that the measured drain current is due to gate leakage in reverse direction.

The measured (squares, left-hand scale) and calculated (circles, right-hand scale) transfer characteristics of the cubic HFET at $V_{DS}=10V$ are depicted in Fig. 14. The calculated data are shifted with respect to the experimental data since the current measured at $V_G=-1V$ is mainly due to gate leakage which has not been included in the simulation. The threshold voltage $V_{th}=0.6V$ was obtained from the intersection of the extrapolated experimental drain current data and the gate leakage line (0.34 mA/mm). Thus, the electron channel at the c-AlGaIn/GaN interface is controlled by positive gate bias. These results demonstrate clearly that cubic AlGaIn/GaN may be used for fabrication of HFETs with normally-off characteristics.

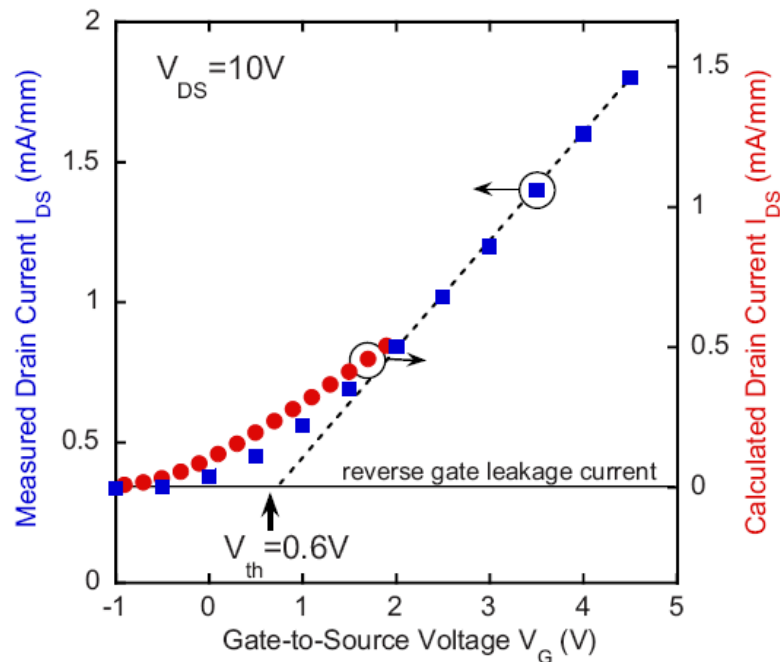


Figure 14: Measured (squares) and calculated (solid circles) transfer characteristics of a cubic $Al_{0.33}Ga_{0.67}N/GaN$ HFET at drain-to source voltage of $V_{DS}=10V$. The right-hand scale of the calculated data is shifted for the value of the reverse gate leakage current of 0.34 mA/mm measured at $V_G=-1V$.

Obviously the first demonstrators of cubic nitride HFETs [61] had output characteristics which are influenced by deficiencies of the structures which are:

a) A large shunt current through the GaN buffer layer.

Capacitance-voltage measurements on nominally undoped cubic GaN revealed a doping concentration in the order of $2 \times 10^{17}cm^{-3}$ yielding a drain current of 0.3mA/mm at $V_G=0V$ and $V_{DS} = 10V$. As a consequence, experiments were performed to reduce the background doping of MBE grown c-GaN. A.Zado et al. [65] used carbon acceptors supplied by an CBr_4 sublimation source connected to the MBE chamber to compensate donors. No carrier gas was used and the CBr_4 flux was set by a high precision needle valve at constant source temperature of 20 °C. They were able to vary the

concentration of incorporated carbon acceptors by more than two orders of magnitude. In this way the concentration of residual donors was compensated and a decrease of the conductance of c-GaN:C by two orders of magnitude was demonstrated.

b) The high gate leakage current of HFETs. It is undesirable for high power and low noise applications, and severely reduces the performance of HFETs.

The use of metal/insulator layers instead of a Schottky gate, leading to the metal-insulator-semiconductor heterojunction field effect transistors (MIS-HFET), may improve the device characteristics [66, 67]. A. Zado et al. [68] have fabricated different MIS structures on cubic GaN. They compared the trap energies and trap densities of devices produced by *ex-situ* plasma enhanced chemical vapor deposition and *in-situ* by molecular beam epitaxy. In the first series the 600 nm thick c-GaN layers were taken out from the MBE chamber and Si₃N₄ layers were deposited by plasma enhanced chemical vapour deposition (PECVD) at a substrate temperature of 300 °C. The pressure during the deposition was 1.33 mbar and the deposition rate was 16 nm/min. The deposited insulator thickness was estimated from the saturation region of the CV curves assuming a dielectric constant of 7.5 for Si₃N₄ [68]. In a second series Si₃N₄ layers were deposited *in-situ* in the MBE chamber after the growth of the c-GaN buffer using the nitrogen plasma source and a silicon thermal evaporation source. The substrate temperature for the deposition of Si₃N₄ layers was 300°C and the growth rate was 13 nm/h. The trap energy and trap densities in MIS structures produced *in-situ* by molecular beam epitaxy and *ex-situ* by plasma enhanced chemical vapor deposition were compared. The MBE produced structure showed a reduced hysteresis effect in the CV curve indicating a lower density of mobile charges. By admittance spectroscopy interface traps were detected between 0.2 eV and 0.4 eV below the conduction band edge with a minimum defect density

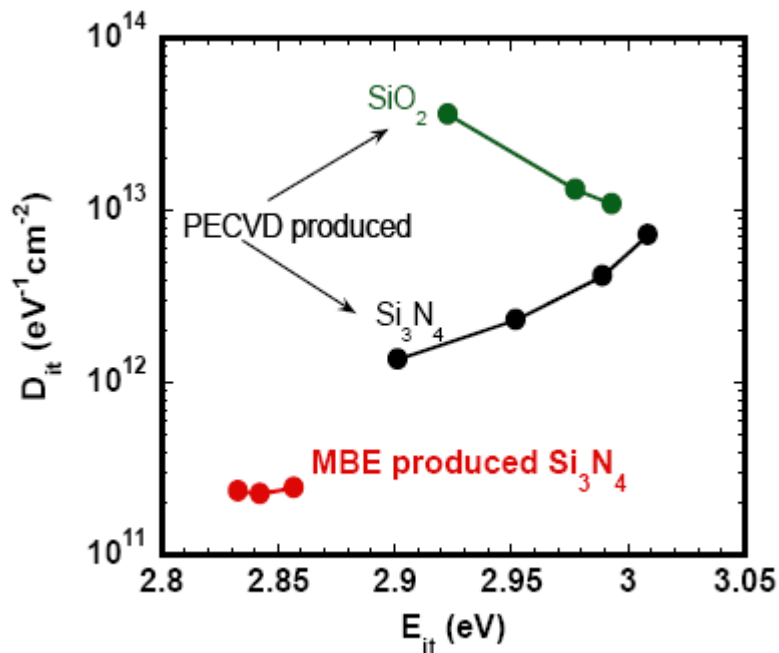


Figure 15: The interface state density D_{it} at the GaN/insulator interface vs. energy E_{it} above the valence band edge of c – GaN.

of $D_{it} = 2.5 \times 10^{11} \text{ cm}^{-2} \text{ eV}^{-1}$ (see Fig. 15). This is more than one order of magnitude lower than in PECVD produced Si_3N_4 structures and two orders of magnitude lower than that measured with SiO_2 insulator layers. These findings demonstrate that MBE produced *in-situ* Si_3N_4 layers can lead to a reasonable decrease of the gate current in further HFET structures.

4. CONCLUSIONS

Recent developments of the in-situ control of growth conditions during the MBE of cubic III-nitrides (GaN/AlN) paved the way to the production of layer stacks with high phase purity and severely improved structural properties. Group III-nitride nanostructures are free of any polarization fields due to their cubic crystal symmetry and therefore may be considered as the true nonpolar group III-nitrides and thus are the ideal material basis of devices where polarization fields are detrimental for their performance. First demonstrators are HFETs with both normally on and normally off operation mode and MQWs for intersubband absorption in the near infrared up to the terahertz spectral region. Their properties are summarized in this paper indicating a clear potential of nonpolar cubic III-nitrides for further applications.

5. ACKNOWLEDGEMENTS

The authors want to thank E. Tschumak, T. Schupp, C. Mietze, A. Zado, S. Potthast, J. Schörmann, and Prof. W.G. Schmidt, and E. Rauls at University of Paderborn, Prof. F. Julien and M. Tchernycheva at University Paris-Sud, Prof. M.O. Manasreh and E. DeCuir, Jr. at Arkansas State University, J. Gerlach at IOM Leipzig, J. Pezoldt, F. Schwierz, and P. Schley at University of Ilmenau and Prof. R. Goldhahn at University of Magdeburg. My special regards are expressed to Dr. M. Abe and Dr. H. Nagasawa at HOYA Corporation, for the supply of excellent 3C-SiC substrates and the financial supply by DFG (project AS 107/4-1 and within the research group “Micro- and Nanostructures in Optoelectronics and Photonics” GRK 1464).

REFERENCES

1. As, D.J., in *Optoelectronic Properties of Semiconductors and Superlattices*, edited by M. O. Manasreh (Taylor & Francis, New York, 2003), Vol.19, Chap. 9, pp. 323–450
2. As, D.J., Potthast, S., Schörmann, J., Li, S.F., Lischka, K., Nagasawa, H., Abe, M., Mater. Sci. Forum **527**, 1489 (2006).
3. Northrup, J.E., Neugebauer, J., Feenstra, R.M. and Smith, A.R., Phys. Rev. B **61**, 9932 (2000).
4. Koblmüller, G., Brown, J., Averbeck, R., Riechert, H., Pongratz, P. and Speck, J. S., Appl. Phys. Lett. **86**, 041908 (2005).
5. Brandt, O., Sun, Y. J., Däweritz, L. and Ploog, K.H., Phys. Rev. B **69**, 165326 (2004).
6. As, D.J., Microelectronics Journal **40**,204 (2009)
7. Schikora, D., Hankeln, M., As, D.J., Lischka, K., Litz, T., Waag, A., Buhrow, T. and Henneberger, F., Phys. Rev. B **54**, R8381 (1996).
8. Feuillet, G., Hamaguchi, H., Ohta, K., Hacke, P., Okumura, H. and Yoshida, S., Appl. Phys. Lett. **70**, 1025 (1997)
9. Neugebauer, J., Zywiets, Z., Scheffler, M., Northrup, J.E. and Van der Walle, C.G., Phys. Rev. Lett. **80**, 3097 (1998).
10. Schörmann, J., Potthast, S., As, D.J., Lischka, K., Appl. Phys. Lett. **90**, 041918 (2007)
11. Mula, G., Adelman, C., Moehl, S., Oullier, J. and Daudin, B., Phys. Rev. B **64**, 195406 (2001).
12. Adelman, C., Brault, J., Jalabert, D., Gentile, P., Mariette, H., Mula, G. and Daudin, B., J. Appl. Phys. **91**, 9638 (2002).
13. Gogneau, N., Sarigiannidou, E., Monroy, E., Monnoye, S., Mank, H. and Daudin, B., Appl. Phys. Lett. **85**, 1421 (2004).
14. Neugebauer, J., Zywiets, T.K., Scheffler, M., Northrup, J.E., Chen, H. and Feenstra, R.M., Phys. Rev. Lett. **90**, 056101 (2003).
15. Lischka, K., phys. stat. sol. (b) **202**, 673 (1997).
16. Yang, H., Brandt, O. and Ploog, K., J. Electr. Mat. **25** (5), 787 (1996).
17. Okumura, H., Ohta, K., Feuillet, G., Balakrishnan, K., Chichibu, S., Hamaguchi, H., Hacke, P., Yoshida, S., J. Crystal Growth **178**, 113 (1997).
18. Yang, H., Zheng, L.X., Li, J.B., Wang, X.J., Xu, D.P., Wang, Y.T., Hu, X.W. and Han, P.D., Appl. Phys. Lett. **74** (17), 2498 (1999).
19. Ayers, J.E., J. Appl. Phys. **78**, 3724 (1995).
20. Daudin, B., Feuillet, G., Hübner, J., Samson, Y., Widmann, F., Philippe, A., Bru-Chevallier, C., Guillot, G., Bustarret, E., Bentoumi G. and Deneuille, A., J. Appl. Phys. **84** (4), 2295 (1998).
21. Daudin, B. and Widmann, F., J. Cryst. Growth **182**, 1 (1997)
22. Lebedev, V., Cimalla, V., Kaiser, U., Foerster, Ch., Pezoldt, J., Biskupek J. and Ambacher, O., J. Appl. Phys. **97**, 114306 (2005)
23. Schupp, T., Rossbach, G., Schley, P., Goldhahn, R., Lischka K. and As, D.J., phys. stat. sol. (c), (2009) (in press).
24. Braun, W., [Applied RHEED], Springer Tracts in Modern Physics, Vol. **154**, Springer, Berlin, (1999)
25. Schörmann, J., As, D.J., Lischka, K., Schley, P., Goldhahn, R., Li, S.F., Löffler, W., Hetterich, M., Kalt, H., Appl. Phys. Lett. **89**, 261903 (2006).
26. Holy, V., [High-Resolution X-Ray Scattering from Thin Films and Multilayers], Springer Tracts in Modern Physics, Vol. **149**, Springer, Berlin, (1999)
27. Cobet, C., Goldhahn, R., Richter, W. and Esser, N. phys. stat. sol. (b), **246**, 1440 (2009).
28. Goldhahn, R., Acta Physica Polonica A **104**, 123 (2003).
29. Röppischer, M., Goldhahn, R., Rossbach, G., Schley, P., Cobet, C., Esser, N., Schupp, T., Lischka, K., and As, D.J., J. Appl. Phys. **106**, 076104 (2009).
30. Leute, R.A.R., Feneberg, M., Sauer, R., Thonke, K., Thapa, S.B., Scholz, F., Taniyasu, Y. and Kasu, M., Appl. Phys. Lett. **95**, 031903 (2009).
31. Bechstedt, F., Seino, K., Hahn, P.H. and Schmidt, W.G., Phys. Rev. B **72**, 245114 (2005).
32. Schörmann, J., Potthast, S., As, D.J., Lischka, K., Appl. Phys. Lett. **89**, 131910 (2006)
33. As, D.J., Potthast, S., Köhler, U., Khartchenko A. and Lischka, K., MRS Symp. Proc. Vol. **743**, L5.4 (2003)
34. Craven, M.D., Waltereit, P., Speck, J.S. and DenBaars, S.P., Appl. Phys. Lett. **84**, 496 (2004).

35. Grandjean, N., Damilano, B., Dalmaso, S., Leroux, M., Lügt, M. and Massies, J., *J. Appl. Phys.* **86**, 3714 (1999).
36. E. A. DeCuir, E. Fred, B. S. Passmore, A. Muddasani, M. O. Manasreh, J. Xie, H. Morkoc, M. E. Ware, and G. J. Salamo, *Appl. Phys. Lett.* **89**, 151112 (2006).
37. D. Hofstetter, E. Baumann, F. R. Giorgetta, M. Graf, M. Maier, F. Guillot, E. Bellet-Amalric, and E. Monroy, *Appl. Phys. Lett.* **88**, 121112 (2006).
38. F. Guillot, E. Bellet-Amalric, E. Monroy, M. Tchernycheva, L. Nevou, L. Doyennette, F. H. Julien, L. S. Dang, T. Remmele, M. Albrecht, T. Shibata, and M. Tanaka, *J. Appl. Phys.* **100**, 044326 (2006).
39. E. Baumann, F. R. Giorgetta, D. Hofstetter, H. Lu, X. Chen, W. J. Schaff, L. F. Eastman, S. Golka, W. Schrenk, and G. Strasser, *Appl. Phys. Lett.* **87**, 191102 (2005).
40. B. K. Ridley, W. J. Schaff and L. F. Eastman, *J. Appl. Phys.* **94**, 3972 (2003).
41. N. Suzuki, N. Iizuka and K. Kaneko, *Japanese J. Appl. Phys., Part 1*, **42**, 132 (2003).
42. I. Vurgaftman, J. R. Meyer and L. R. Ram-Mohan, *J. Appl. Phys.* **89**, 5815 (2001).
43. Hadis Morkoc, in *Nitride Semiconductors and Devices (Springer Series in Materials Science)*, (Springer-Verlag, 1999), Vol. **132**, p. 488.
44. T. G. Andersson, X. Y. Liu, T. Aggerstam, P. Janes, P. Holmstrom, S. Lourdudoss, and L. Thylen, *J. Cryst. Growth*, **301-302**, 457 (2007).
45. O. Ambacher, R. Dimitrov, M. Stutzmann, B. E. Foutz, M. J. Murphy, J. A. Smart, J. R. Shealy, N. G. Weimann, K. Chu, M. Chumbes, B. Green, A. J. Sierakowski, W. J. Schaff, and L. F. Eastman, *Phys. Stat. Sol. B* **216**, 381 (1999).
46. S.-H. Park and S.-L. Chuang, *Appl. Phys. Lett.* **76**, 1981 (2000).
47. C. Gmachl and H. M. Ng, *Electron. Lett.* **39**, 567 (2003).
48. E. Kuokstis, W. H. Sun, C. Q. Chen, J. W. Yang, and M. A. Khan, *J. Appl. Phys.* **97**, 103719 (2005).
49. E.A.DeCuir, Jr., M.O. Manasreh, E. Tschumak, J. Schörmann, D.J. As and K. Lischka *Appl. Phys. Lett.* **92**, 201910 (2008)
50. H. Machhadani, M. Tchernycheva, L. Rigutti, S. Saki, R. Colombelli, C. Mietze, D.J. As and F.H. Julien *Phys. Rev. B* **83**, 075313 (2011).
51. A. Helman, M. Tchernycheva, A. Lusso, E. Warde, F. H. Julien, K. Moumanis, G. Fishman, E. Monroy, B. Daudin, L. S. Dang, E. Bellet-Amalric, D. Jalabert, *Appl. Phys. Lett.* **83**, 5196 (2003).
52. M. Tchernycheva, L. Nevou, L. Doyennette, F. H. Julien, E. Warde, F. Guillot, E. Monroy, E. Bellet-Amalric, T. Remmele, M. Albrecht, *Phys. Rev.* **73**, 125347 (2006).
53. F. H. Julien, M. Tchernycheva, L. Nevou, L. Doyennette, R. Colombelli, E. Warde, F. Guillot, E. Monroy, *Phys. Stat. Sol. A* **204**, 1987 (2007.)
54. T. Unuma, M. Yoshita, T. Noda, H. Sakaki, H. Akiyama, *J. Appl. Phys.* **93**, 1586 (2003).
55. M. Tchernycheva, L. Nevou, L. Doyennette, F. H. Julien, E. Warde, F. Guillot, E. Monroy, E. Bellet-Amalric, T. Remmele, M. Albrecht, *Phys. Rev.* **73**, 125347 (2006).
56. C. Mietze, M. Landmann, E. Rauls, H. Machhadani, S. Sakr, M. Tchernycheva, F.H. Julien, W.G. Schmidt, K. Lischka and D.J. As, *Phys. Rev. B* **83**, 195301 (2011).
57. S. Rajan, P. Waltereit, C. Poblentz, S. J. Heikman, D. S. Green, J. S. Speck and U. K. Mishra, *IEEE Electron Device Lett.* **25**, 247 (2004).
58. S. Haffouz, H. Tang, J. A. Bardwell, E. M. Hsu, J. B. Webb, and S. Rolfe, *Solid-State Electron.* **49**, 802 (2005).
59. Y. C. Choi, J. Shi, M. Pophristic, M.G. Spencer, and L.F. Eastman, *J. Vac. Sci. Technol. B* **25**, 1836 (2007).
60. M. Abe, H. Nagasawa, S. Potthast, J. Fernandez, J. Schörmann, D. J. As and K. Lischka, *IEICE Trans. Electron.* **E89-C**, 1057 (2006).
61. E. Tschumak, R. Granzer, J.K.N. Lindner, F. Schwierz, K. Lischka, H. Nagasawa, M. Abe, and D.J. As *Appl. Phys. Lett.* **96**, 253501 (2010).
62. M. Kuroda, H. Ishida, T. Ueda, and T. Tanaka, *J. Appl. Phys.* **102**, 093703 (2007.)
63. ATLAS User's Manual—Device Simulation Software, Silvaco International, 2008.
64. D. J. As, S. Potthast, J. Schörmann, S. F. Li, K. Lischka, H. Nagasawa, and M. Abe, *Mater. Sci. Forum* **527–529**, 1489 (2006).
65. A. Zado, E. Tschumak, J. Gerlach, K. Lischka, and D.J. As, *J. Crystal Growth* **343**, 88 (2011).
66. V. Adivarahan, J Yang, A. Koudymov, G. Simin, and M. Asif Khan, *IEEE Electron. Dev. Lett.* **26**, 535 (2005).
67. R.B. Gila, F. Ren, and C.R. Abernathy, *Mater Sci. Eng.* **R 44**, 151 (2001).
68. A. Zado, K. Lischka and D.J. As, *phys. stat. sol. (c)* (2011) (to be published).